ORIGINAL ARTICLE

Cytometry PART A
Journal of the International Society for Advancement of Cytometry

Measurement and Autocorrelation Analysis of Two-Dimensional Light-Scattering Patterns from Living Cells for Label-Free Classification

Yong-Le Pan,[1]* Matthew J. Berg,[1,2] Samuel Shao-Min Zhang,[3] Heeso Noh,[4] Hui Cao,[4] Richard K. Chang,[4] Gorden Videen[1]

[1]U. S. Army Research Laboratory, Adelphi, Maryland 20783

[2]Department of Physics and Astronomy, Mississippi State University, Mississippi State, Mississippi 39762

[3]Department of Neural and Behavioral Sciences, Penn State Milton S. Hershey Medical Center, Hershey, Pennsylvania 17033

[4]Department of Applied Physics, Yale University, New Haven, Connecticut 06520

Received 12 April 2010; Revision Received 12 January 2011; Accepted 3 February 2011

Grant sponsor: NSF; Grant number: DMR-0808937; Grant sponsors: Defense Threat Reduction Agency (Physical Science and Technology Basic Research Program), the US Army Research Laboratory mission fund, Penn State University Start-up Funds.

*Correspondence to: Yongle Pan, U. S. Army Research Laboratory, Adelphi, Maryland 20783, USA

Email: yongle.pan@arl.army.mil

Published online 8 March 2011 in Wiley Online Library (wileyonlinelibrary.com)

DOI: 10.1002/cyto.a.21036

• Abstract

We incorporate optics and an ICCD to record the two-dimensional angular optical scattering (TAOS) patterns retrieved from single aerosolized cells. We analyze these patterns by performing autocorrelations and demonstrate that we are able to retrieve cell size from the locations of the secondary maxima. Additional morphological information is contained in the autocorrelation functions and decay rate of the heights of the autocorrelation peaks. We demonstrate these techniques with C6 and Y79 cells, which are readily distinguishable. One key advantage of this methodology is that there is no requirement for antibody and fluorescent labeling molecules. Published 2011 Wiley-Liss, Inc.†

• Key terms

elastic scattering pattern; autocorrelation; label-free; cell

CELL-BASED therapies are being used increasingly in modern clinical practices, from bone-marrow transplantation to stem-cell replacement. The demands on sensitivity for cell classification and identification are continually increasing. Flow cytometry has developed into one of the key techniques for counting, analyzing, and sorting microscopic particles, such as cells and chromosomes. It is used widely in molecular biology, pathology, immunology, and other fields, such as diagnosing disordered blood cancers in pathology. Flow cytometry is used to classify particles in the sub- to super-micron size range by examining the intensities of fluorescence and elastic scattering when particles move through a fluidic system. Information is captured from one or more fluorescence bands at different wavelength regions and from an elastic scattering channel located at one or several scattering angles, usually at intermediate and near-forward scattering angles. The cells may also be illuminated by one or more lasers, depending on the application. Fluorescence emissions typically result from fluorescent molecular markers that attach to specific antibodies for specific cell labeling, but can also result from intrinsic fluorescence (often called autofluorescence) of the examined cell itself. Different kinds of cells can be well discriminated, identified, and sorted using such techniques (1–5).

One recent advance is the use of polychromatic approaches that have entered the mainstream in flow cytometry (6,7). Instruments for measuring 17 bands of fluorescence and two parameters of elastic scattering using multiple laser excitations have been reported (7). Other advances include introducing image-intensified charge coupled devices (ICCDs) to record the dispersed fluorescence spectrum (6), and using photo-diodes, avalanche diodes (APD), or photomultiplier tube (PMT) (8–10) linear arrays as spectral detectors. Using the dispersed fluorescence spectrum can improve the accuracy and precision of ratiometric measurements and increase the probability of recording more discrete fluorescence bands.

The fluorescence metric measurement is a powerful means to identify cells. However, the introduction of costly labeling fluorescent molecules can be an impediment. These may require further cell culture, analysis, and confirmation by biological molecular diagnostics after being sorted, such as from bone-marrow transplantation to stem-cell replacement. Recent advances in analyzing elastic scattering patterns and UV-laser induced fluorescence spectra (8–14) are providing information on aerosol particle morphology, such as size, refractive index, absorption, shape, asymmetry factor, surface roughness, or whether there are inclusions (12). This has encouraged us to apply these techniques to a label-free, cell-classification flow cytometer. The advanced technologies, such as the multiple-anode PMT (Hamamastu with 1 × 16, 1 × 32, or 8 × 8 anodes) and related electronics (Vertilon) has enabled us to record and analyze the spectrum or images at rates exceeding several 10 k particles per second. The use of fast computer and differential algorithms are helping in the extraction of information from the scattering patterns.

In 1975, Salzman et al. reported extracting useful information from a 32-parameter multiangle scattering flow cytometer (15). Wyatt et al. used multiangular scattering information to identify living bacterial cells (16). Recently, Maltsev (17) and Semyanov et al. (18) developed a scanning flow cytometer to record continuous phase functions of cells. However, the scattering intensity distribution also varies in the azimuthal direction φ, which can be used to provide additional information about cell asymmetry. Two-dimensional angularly resolved scattering patterns capture this additional information, which can be used in particle characterization (11–14). The inverse problem of extracting morphological information directly from the scattering patterns is extremely difficult. Completely characterizing a particle from the light-scattering information is an intractable problem; however, some information is readily available. For instance, information can be obtained about particle size and shape using forward diffraction (19). Information about absorption and agglomeration of a particle system can be obtained from the backscattering region (20). Scattering patterns from single *Bacillus subtilis* spores are in good agreement between experimental measurement and theoretical simulations (21).

In this manuscript we use the autocorrelation of scattering patterns measured from single-cells to obtain information about the cellular structure. Although there are numerical studies related to elastic scattering and autocorrelation calculations, such as from particles in suspension (22), rough surfaces (23,24), polymer films (25), semicontinuous metal films (26) and random-lasing emission (27), this is the first report that we know of in which autocorrelation calculations are applied to two-dimensional angularly resolved optical scattering (TAOS) patterns to obtain information about a single cell, and also the first report that we know of in which TAOS patterns are measured from a single moving cell. We use this analysis to extract size and shape related information from the TAOS patterns obtained from rat cells C6 and human cells Y79. Our studies demonstrate that they are well discriminated by the autocorrelation parameters extracted from the TAOS patterns.

Experimental Method and Autocorrelation Analysis

Sample Cell Preparation

Both C6 and Y79 cells used in this study were purchased from ATCC (Manassas, VA). C6 cells, an adherent rat glial tumor cell line, were cultured in the DMEM/F12 (Invitrogen, CA) medium with 10% fetal bovine serum (Atlanta Biologicals, GA). Y79 cells, a suspension human retinoblastoma cell line, were cultured in the RPMI-1640 (Invitrogen, CA) medium with 20% fetal bovine serum (Invitrogen, CA). All cells were cultured in a 37.0°C incubator with 95% air and 5% carbon dioxide. Cells were dissociated with 0.05% Typsin contained EDTA•4Na (Invitrogen, CA) for 5–10 min at 37.0°C. Then the cells were suspended into single cells and centrifuged down to remove the culture medium at 800 rpm. Half of the cells (about 500,000) from both cell types were re-suspended and moved to new tubes with 5 ml of their original medium without serum for analysis, respectively. Half of the cells were resuspended and fixed in 2% paraformaldehyde (Electron Microscopy Sciences, PA) in 1 × PBS for 10–15 min and then centrifuged at 800 rpm to remove the fix solution. The cells then were resuspended with 1x PBS for analysis. The cells from different stages of preparation were imaged by an inverted microscope (Olympus, PA) equipped with a Spot digital camera (Spot Image Solution, MI). Figure 1 shows the microscopic phase-contrast images of the two types of cells at different stages. A 40X, NA = 0.5 microscopy objective has been used. Both cells have a sphere-like shape, are around 6 ∼ 7 μm in diameter after being dissociated. The C6 cells appear to have a rougher surface structure. It appears that the C6 cells is slightly larger than the Y79 cells based on the middle images, but it might be caused by the focusing errors of microscopy.

Experimental Arrangement

The experimental setup is a modification of that of Pan et al. (13)., who measured the light-scattering patterns from bio-aerosol particles. The simplified schematic of the experimental arrangement is shown in Figure 2a. An inkjet aerosol generator produces a stream of droplets ∼50 μm in diameter containing buffer fluid and cells (31). The cell concentration within the buffer fluid is dilute enough that the volume of five droplets contains one cell on average; therefore, most droplets contain only one cell or none. Once these droplets fall through a drying column, the buffer liquid evaporates and its moisture is carried away by a dry air flow, leaving bare cells. The temperature and dry air flow rate are tested to evaporate the buffer fluid without drying the cell itself. Microscopy images confirmed that these cells collected after passing the drying column remain the similar shapes and sizes as that shown in Figure 1.

Cells are focused to a stream of 300 μm in diameter by an aerodynamic sheath nozzle (10) and traverse the focal volume of a prolate ellipsoidal mirror. The mirror is custom designed with a major axis of 3.5″ and eccentricity of 0.70. Holes were drilled in the ellipsoid to accommodate the laser beam and cell stream so that both can intersect one of the foci as shown in

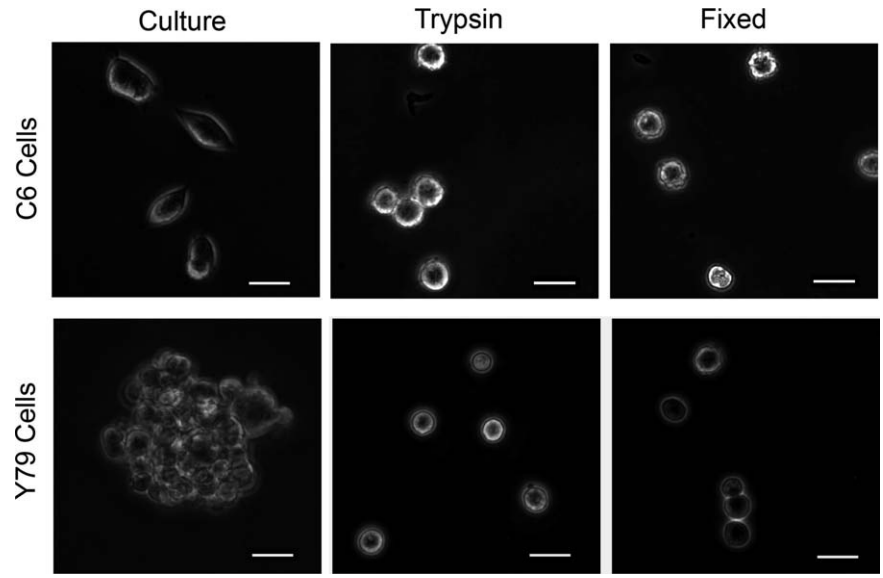

Figure 1. Microscopic phase-contrast images of adherent rat glial tumor cells C6 (top) and human retinoblastoma cells Y79 (bottom). The white bar in each image represents 10 μm. The first column shows the cultured C6 cells by DMEM/F12 medium with 10% fetal bovine serum and Y79 cells by RPMI-1640 medium with 20% fetal bovine serum. The middle column shows these cells dissociated with 0.05% Typsin contained EDTA•4Na (Invitrogen, CA) for 5—10 min at 37.0°C, centrifuged and suspended into single cells. The right column shows these cells centrifuged and resuspended after being fixed in 2% paraformaldehyde in 1 × PBS.

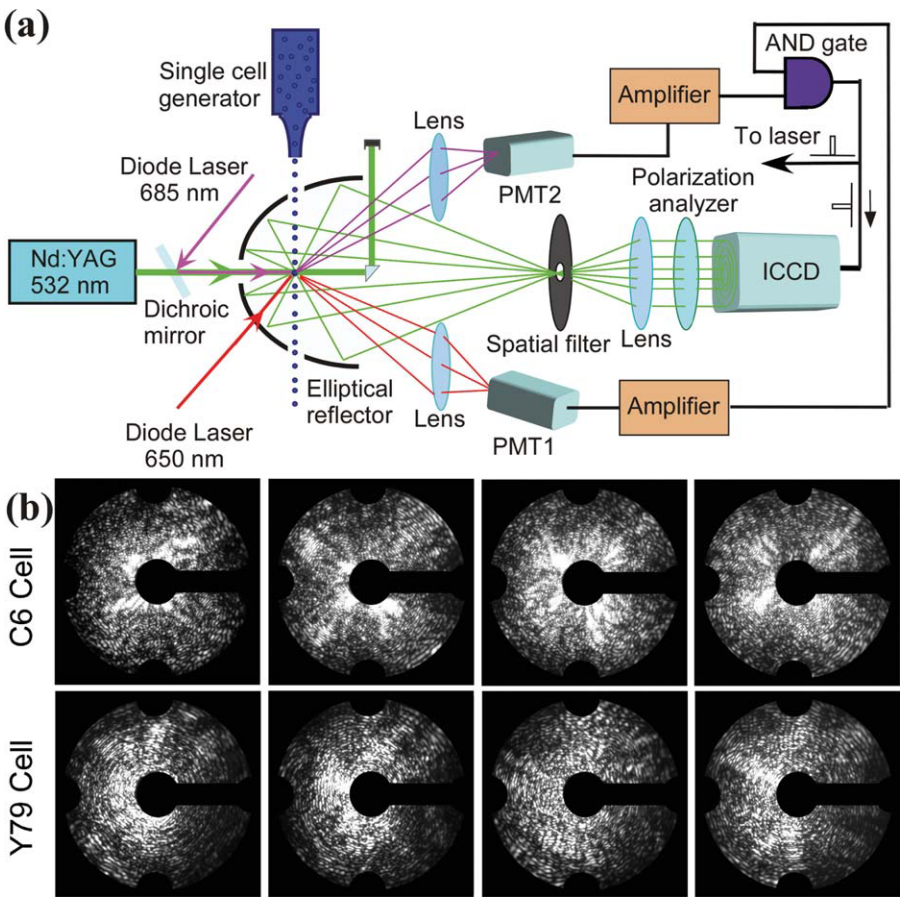

Figure 2. (**a**) The schematic of the experimental arrangement for measuring two-dimensional angular optical scattering (TAOS) patterns from single moving cells by a single laser pulse. Key components are: (1) single cell generator; (2) two cw diode lasers (at 635 nm and 685 nm) and corresponding photomultiplier tubes (PMT) to detect the presence of cells; (3) a *Q*-switched ns pulse laser (532 nm) to illuminate the aerosols; (4) an ellipsoidal reflector to collect the scattered light from the backward hemispheric direction; (5) a camera lens (*f*-number, 1.2; $f = 55$ mm) to project the scattered light to a plane; and (6) an ICCD camera to record the scattering pattern. (b) Raw two-dimensional angular optical scattering (TAOS) patterns $I(x,y)$ from single individual C6 cells (top) and Y79 cells (bottom). [Color figure can be viewed in the online issue, which is available at wileyonlinelibrary.com.]

Figure 2a. Before entering the ellipsoidal mirror system, the droplets pass through a crossed-beam trigger system (10,14) that is used to detect when a cell is on a trajectory that will pass through the mirror focus. Two CW diode-laser beams (650- and 685-nm) are aligned so that the intersection on this trajectory is approximately a 150 μm diameter cross section. Two PMTs (Hamamatsu H6780-02) detect the scattered light from particles passing through these beams. One PMT is equipped with an interference filter to pass 650-nm and the other PMT is equipped with an interference filter to pass 685-nm wavelength light to match the two diode lasers. If the PMTs simultaneously detect scattered light beyond a preset threshold, a particle most likely has entered the trigger volume. When signals on both PMTs exceed a preset threshold, an AND gate triggers a pulsed 532-nm laser and the detection system composed of a pulsed laser (Spectra Physics X-30) and ICCD (Andor IStar). In addition, the CW diode trigger beams are switched off, preventing this unwanted stray light from reaching the ICCD during the "on" time.

The crossed-beam trigger system described above effectively reduces the errors due to off-axis aberrations, such as coma by limiting the sample volume to approximately (150 μm) (3) defined by the crossed diode lasers, which is considerably smaller than the cell stream (300 μm in diameter). These aberrations deform the scattering pattern and also lead to uncertainty in labeling the scattering angle in the pattern. Because there is a time delay between when the particle passes the trigger volume and when the pulsed laser and detector can be activated, the trigger volume is located approximately 20 μm above the focus of the elliptical mirror.

The pulsed laser is focused and collimated to be approximately planar and 1-mm in diameter (20 μJ/pulse, 30-ns pulse duration, 532 nm-2nd harmonic of Nd:YAG). By use of a *Q*-switched laser instead of a CW laser, the individual cell, traveling at $\sim$ 10 m/s, is spatially frozen during the 30-ns pulselength, resulting in a high quality scattering pattern. Scattered light originating from a cell located at the focal point of this mirror is reflected to the second focal point, where a spatial filter is located to remove stray light. It continues to the 1,024 $\times$ 1,024 two-dimensional ICCD detector, which is located in the far-field of the scattering volume. The incident laser beam is reflected to the side by a 2 mm rectangular prism where it is captured by a beam stop, and any forward scattering that is not reflected from this prism is blocked by the spatial filter (an iris 1 mm in diameter). By taking into account the geometry of the system, every pixel of the detector can be matched with a unique scattering angle (polar angle θ and azimuth angle ϕ). The laser propagation direction is defined to be the positive *z*-axis and coincides with the long-axis of the ellipsoidal mirror. This configuration collects a large solid angle ($75^o < \theta < 165^o$, $0^o < \phi < 360^o$) of scattered light, and allows capture of nearly the entire backward hemisphere of scattered light. By swapping the positions of the laser and beam stop, we can capture the scattering in the forward direction. The laser is vertically polarized. By placing a polarization analyzer in the front of the ICCD, we can record either the perpendicular or the parallel polarization scattering patterns. The system was tested and calibrated by measuring the TAOS patterns from 2 and 5 μm polystyrene microspheres (Duke scientific). The experimental data are unwrapped as described below and show very good agreement with Mie calculations.

Autocorrelation Properties from TAOS Patterns of Cells

The ICCD records the two-dimensional intensity distribution at each pixel in a 1,024 $\times$ 1,024 data matrix, $I(x, y)$. The pattern is unwrapped into a format that can be compared with theoretical simulations. We perform the autocorrelation calculation in four steps as follows: (1) the $I(x, y)$ intensity pattern is projected onto a spherical coordinate system $I(\theta,\varphi)$ through a ray-tracing program (2). As the pattern $I(\theta,\varphi)$ is now irregularly spaced with different variation step at θ and ϕ between each pixels, a new intensity matrix with uniformly spaced angles is generated, $I'(\theta,\varphi)$, which covers $94^o < \theta < 144^o$, $0^o < \phi < 360^o$ as a 278 $\times$ 2,000 intensity matrix with a 0.18^o angle variation step. Each intensity $I'(\theta,\varphi)$ is generated by inverse distance-weighted interpolation (28) from the five nearest data points (3). As the scattering intensities from a single cell near the backward direction ($\theta \sim 180^o$) has generally much stronger intensity than that at midrange angles $\theta \sim 90^o$, the backscattered enhancement can dominate the autocorrelation calculations. To remove this artifact, we perform a background subtraction process: the weakest intensity within the nearest 15 $\times$ 15 data matrix is found at each data point, then a matrix formed by these intensities are smoothed by cubic spline to form a background matrix $B(\theta, \phi)$ with 278 $\times$ 2,000 data points. This background matrix is subtracted from $I'(\theta,\varphi)$ at each data point; i.e., $I''(\theta,\varphi) = I'(\theta,\varphi) - B(\theta,\varphi)$. This process is repeated three times on the subsequent matrices to produce the final processed matrix $I^f(\theta,\varphi)$ with 278 $\times$ 2,000 data points. This new $I^f(\theta, \phi)$ has less peak intensity difference between angles θ near 180^o and 90^o, yet preserves the spatial features within the scattering pattern (4). The autocorrelation function is calculated as

$$\mathrm{Corr}\ (\Delta\theta, \Delta\varphi) = \frac{\langle I^f(\theta, \varphi) I^f(\theta + \Delta\theta, \varphi + \Delta\varphi)\rangle}{\langle I^f(\theta, \varphi)\rangle^2} - 1 \qquad (1)$$

Results

One hundred light-scattering patterns from single aerosolized cells are recorded in the perpendicular polarization state from single individual cells of either C6 or Y79. Figure 2b show four typical patterns from C6 (upper row) and Y79 cells (lower row). While the scattering patterns of spherical particles are composed of concentric rings, the ring-like features displayed in some of these patterns are broken with irregular island-shapes. They are similar to those of perturbed spheres and aggregates of spherical particles that we measured from complex atmospheric aerosols (13,14). In examining many of these patterns, we are unable to distinguish between the two categories of patterns by eye, except there appears to be a slightly smaller peak separation along the θ direction and less continuity of broken rings from C6 cells than from Y79 cells.

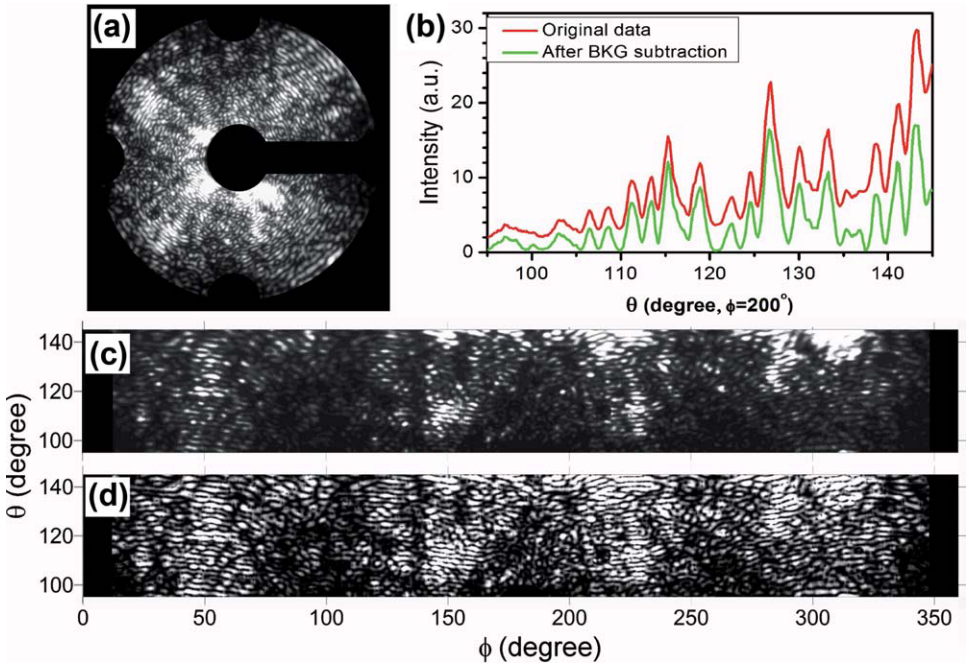

Figure 3. (**a**) A typical TAOS pattern from a single C6 cell in original data form $I(x,y)$. (**b**) Effect of subtracting out the background. Red (upper) line: the raw original scattering intensity distribution from $\theta = 94^{\circ}$ to $\theta = 144^{\circ}$ at $\phi = 200^{\circ}$. Green (lower) line: the corresponding scattering intensity distribution after background subtraction. (**c**) TAOS pattern $I'(\theta, \varphi)$ mapped from (a). (**d**) Scattering pattern $I^{f}(\theta, \varphi)$ after the background subtraction. [Color figure can be viewed in the online issue, which is available at wileyonlinelibrary.com.]

Figure 3 shows one example of how we interpreted the scattering pattern from a C6 cell. The original data in $I(x, y)$ are shown in Figure 3a. Figure 3b shows the effect of subtracting out the background. Figure 3c shows the TAOS pattern $I'(\theta,\varphi)$ mapped from the intensity distribution at ICCD pixels $I(x,y)$ from Figure 3a. Figure 3d shows the scattering pattern $I^{f}(\theta,\varphi)$ after the background subtraction, which has much less peak-to-valley intensity difference throughout the angular range, but preserves the spatial information.

Two-dimensional autocorrelation as a function of shift angles $\Delta\theta$ and $\Delta\phi$ are calculated from the scattering patterns of 100 C6 and 100 Y79 cells. Some periodic structure is apparent in the result, especially near $\Delta\theta = 0$ and $\Delta\phi = 0$. To our surprise, the features contained in the autocorrelations of the scattering patterns of 100 individual C6 cells or that of 100 Y79 cells are quite similar. Figure 4a show the cross-section of the autocorrelations at $\Delta\phi = 0$ calculated from the scattering patterns of 16 C6 cells (left) and 16 Y79 cells. Among them, eight from the first fixed cells and eight from the trypsin cells. We see very little difference between these cells treated using two methods. The location of the first minimum is usually called the correlation length and is a measure of the lateral scale of the scattering pattern (23). The periodic oscillation (the $\Delta\theta$ value from peak to peak) is approximately twice the correlation length. This spacing corresponds to the average separation between the adjacent scattering peaks along the $\Delta\theta$ direction. Figure 4a shows that all have a 1.2° correlation length, and the second maximum appears at 2.1° along the $\Delta\theta$ direction for C6 cells. The maxima shift from cell to cell but remain within a reasonably constrained region. The averaged periodic oscillation spacing from the first four maxima of the 16 C6 cells is 2.04 ± 0.16 (see the inset). Complementary autocorrelation parameters for Y79 cells show similar consistencies among individual cells, but significantly different characteristics from those of the C6 cells. The average periodic oscillation spacing from the first three maxima of the 16 Y79 cells is 2.73 ± 0.33, and the second maximum is located at $\Delta\theta = 2.78 \pm 0.12$. There is no overlap between the second maxima of the C6 and Y79 cells for the 100 measurements for each type of cells.

Because of the variation of these spacings, the oscillation is gradually dampened and the autocorrelation peaks are broadened and shifted when $\Delta\theta$ increases. Figure 4b shows how the amplitudes of these maxima decay as $\Delta\theta$ increases. We fit this plot to a decaying exponential and find the decay rate to be 1.78 ± 0.19 for C6 cells and 1.66 ± 0.28 for Y79 cells. This value is a measure of the spatial periodicity. The larger this value, the more periodic the structure. That a slightly faster decay rate for Y79 cells than the C6 cells reveals a slightly worse correlation between the scattering patterns from the Y79 cells than that from the C6 cells.

Autocorrelations at $\Delta\theta = 0$ are shown in Figure 4c. There are some weak periodic oscillations with a spacing of approximately 8–15°, which corresponds to an average peak-to-peak separation in the ϕ direction, or the averaged size of the intensity islands. The larger variation of the pattern spacing along the ϕ direction results in a weaker correlation, with less peak and value contrast than that along the θ direction. The degree

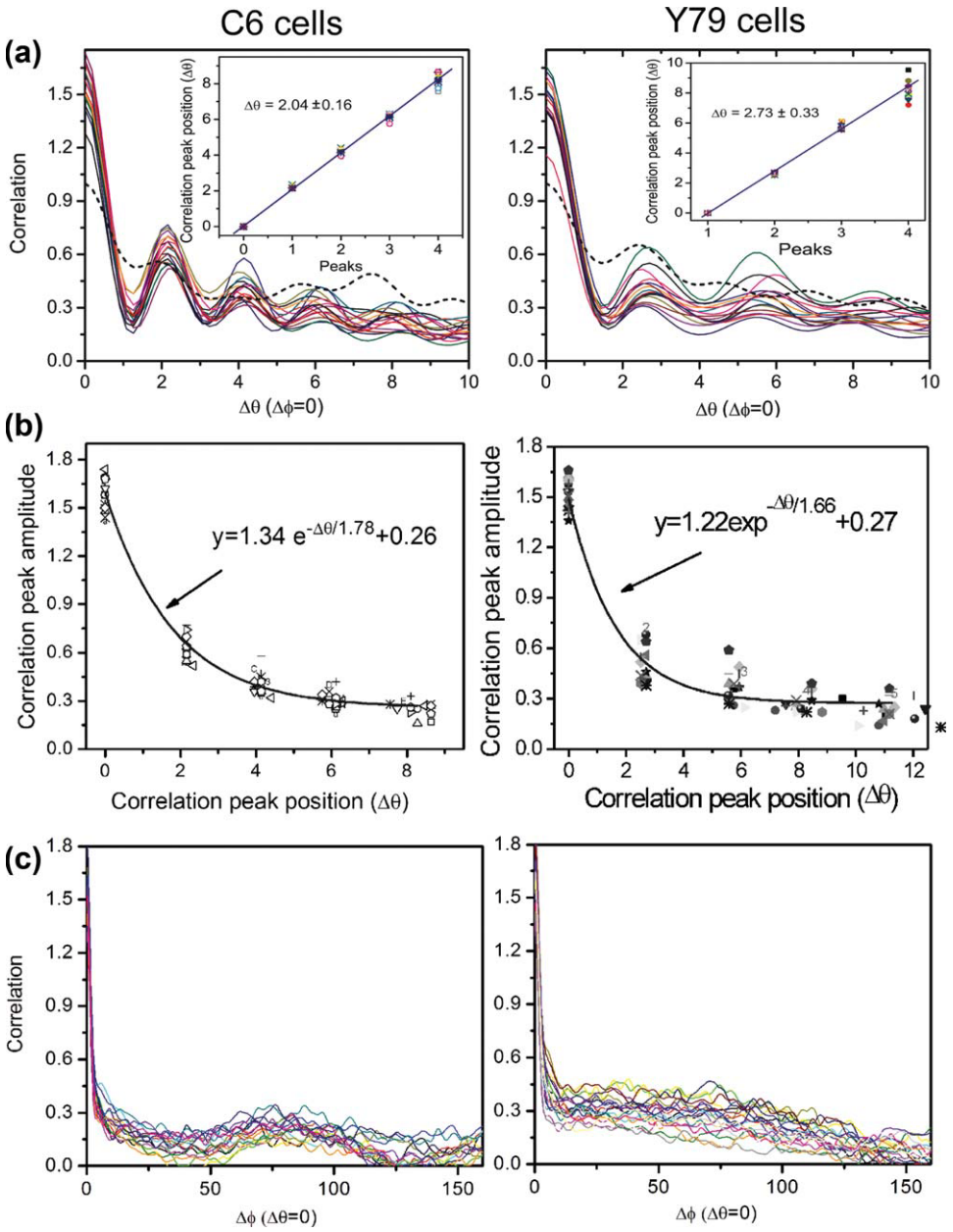

Figure 4. (**a**) One-dimensional autocorrelation from 16 individual C6 and Y79 cells as a function of $\Delta\theta$ at $\Delta\phi = 0$, shown as solid lines. The dashed curves in each plot show the simulated autocorrelation for a sphere of diameter 7.6 μm in C6 and 6.4 μm in Y79 cells. The inset shows that the correlation peak positions vary from cell to cell as $\Delta\theta$ increases, but the location of the second peak appears little invariant. (**b**) Amplitude of autocorrelation maxima as a function of correlation maxima position $\Delta\theta$ for C6 and Y79 cells. The line is a least-square fit to an exponential function. (**c**) One-dimensional autocorrelation from 16 individual C6 and Y79 cells as a function of $\Delta\varphi$ at $\Delta\theta = 0$. [Color figure can be viewed in the online issue, which is available at wileyonlinelibrary.com.]

of breakdown of the ring patterns are mostly from the contribution of nonuniformity inside of the cell and the surface roughness. In addition to this high-frequency oscillation, there is a very strong periodic structural signature with a spacing of approximately 75° for C6 cells. Very low angular frequencies in the scattering are the result of high-spatial frequency structure on the particle. Strong peaks are indicative of these C6 cells having a distinct shape with some drift away from a sphere towards a cube, or recognizable structural features from a sphere (29). However, there is no low-frequency oscillation for the Y79 cells, like that seen at ~75° for C6 cells. This indicates that the Y79 cells are close to a spherical shape.

Theoretical Calculations of TAOS Patterns for Model-Cells

To analyze the measured TAOS autocorrelation functions presented in the previous section, we make comparisons with

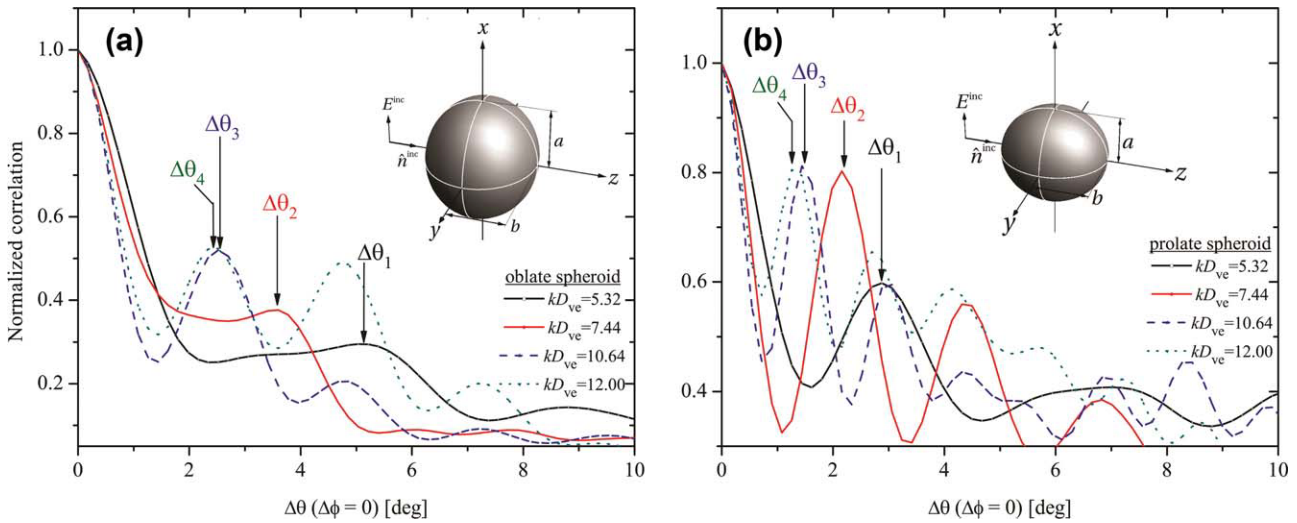

Figure 5. Size dependence of the calculated autocorrelation function for (**a**) oblate- and (**b**) prolate-spheroidal model cells. The secondary-peak positions for each cell are labeled $\Delta\theta_1$-$\Delta\theta_4$ and plotted below in Figure 6a. One can see the inverse relationship between cell size and peak position. [Color figure can be viewed in the online issue, which is available at wileyonlinelibrary.com.]

autocorrelation functions calculated from model cells. We use the T-Matrix code (30) to simulate the light-scattering patterns for these cells. The images in Figure 1 suggest a rounded particle whose major axis is ∼10% longer than its minor axis, suggesting that we can approximate the cell shape to be either an oblate or prolate spheroid. These model cells are characterized by their volume-equivalent-sphere diameter D_{ve} and aspect ratio a/b. If a/b is greater than one, the shape is oblate, and if a/b is less than one, then it is prolate. Examples of these model cell shapes are shown in Figure 5. The cells are illuminated by a linearly polarized plane wave with a wavelength of 532 nm with the same geometry used in the measurements. The refractive index of the cells is taken as $m = 1.4 + 0.002i$ following the estimates for human red blood cells given (31). Using the T-Matrix code, the far-field scattered light intensity is calculated over the same two-dimensional angular range as the measured TAOS patterns. Once the scattering patterns are calculated, the same background subtraction, as described in Section Autocorrelation properties from TAOS patterns of cells, is performed to accentuate the pattern's ripple structure. From this background-modified pattern, the autocorrelation function is calculated and compared to the measured functions as described below.

Figure 5a shows the normalized autocorrelation function for oblate model cells with an aspect ratio of $a/b = 1.1$ and sizes ranging from $D_{ve} = 5.32$ to 12.0 μm. The autocorrelation shows the same peaked structure as in Figure 4a. As the size of the cell increases, the positions of the peaks move toward smaller $\Delta\theta$. The secondary peak for each cell is labeled on the curves as, $\Delta\theta_1$, $\Delta\theta_2$, $\Delta\theta_3$, and $\Delta\theta_4$. Figure 5b shows the autocorrelation function for prolate model cells with an aspect ratio $a/b = 0.9$ and sizes identical to those of Figure 5a. Here again, one can see that the larger the cell size, the more the peaks become shifted to smaller angles. We examine the secondary-peak location to establish if it contains a functional relationship that can be used to obtain cell size. Figure 6a shows a log-log plot of the secondary-peak positions as a function of the cell size parameter kR_{ve}, where k is the vacuum wavenumber and R_{ve} is the sphere-volume-equivalent radius. One can see that the peaks $\Delta\theta_1$, $\Delta\theta_2$, $\Delta\theta_3$, and $\Delta\theta_4$ for both the oblate and prolate cell-shapes fall on a line with slope of negative one. For the nearly spherical particles in this study, this indicates an inverse relationship between the secondary-peak position and the cell size, i.e.,

$$\Delta\theta = \frac{c}{kR_{ve}} \tag{2}$$

where c is a constant particular to a given cell shape and orientation, but is independent of cell size. The meaning of this simple relationship is that the average angular width of the ripple-structure of the scattering pattern in the θ-direction is inversely related to the cell size-parameter. A similar relationship is described for spherical shapes in (32).

Besides cell size and shape, its orientation with respect to the incident light is an important variable affecting the structure of the scattering pattern. Indeed, the measurements are performed on cells in fixed, arbitrary orientations. Figure 6b shows the autocorrelation function for the same $D_{ve} = 10.64$ micron prolate model cell as in Figure 6b, except here the orientation is varied as shown by the inset diagrams. One can see that the second peaks of the autocorrelation curves occur at approximately the same location, with primary variations only in their amplitude, but the third peaks start to vary from cell to cell. This behavior is consistent with the measurements presented in Figure 4a, and indicates that cell orientation largely does not affect the inverse relationship between the secondary-peak position $\Delta\theta$ and size parameter kR_{ve}. Moreover, the dependence of the peak location on the assumed cell shape appears to be much weaker than the size dependence.

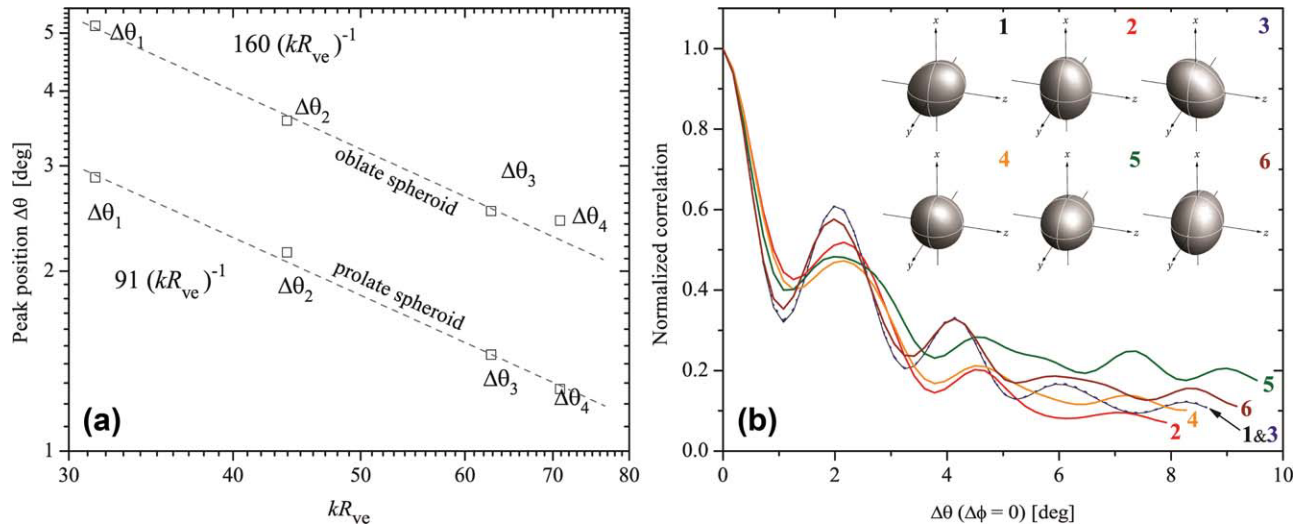

Figure 6. (**a**) Inverse relationship between secondary-peak location and model-cell size parameter. The points labeled $\Delta\theta_1$-$\Delta\theta_4$ correspond to the peak locations in Figure 5**b**. Orientation dependence of the autocorrelation function for the D_{ve} = 10.64 prolate model cells in Figure 5b. The orientations are shown in the inset diagrams. One can see that the position of the secondary peak is largely independent of cell orientation. [Color figure can be viewed in the online issue, which is available at wileyonlinelibrary.com.]

This can be seen in Figure 4a where the calculated autocorrelation curves (dashed lines) for a sphere of diameter 7.6 and 6.4 μm along with the measured curves. These sizes are estimated from Figure 6a for a prolate spheroid. The location of the secondary peak for the calculated and measured curves is approximately the same. Thus, both a prolate spheroid and sphere model-cell give a secondary-peak at the same location provided that they share the same sphere-volume-equivalent diameter. In addition, the explicit diameters used for the calculated curves in Figure 4a are consistent with the actual-cell size estimated from the microscope images in Figure 1. In addition, the calculated autocorrelation curves show that amplitudes of these maxima decay much slower than the measured data as $\Delta\theta$ increases, it also implies that decay rate represents how far away the real cell is from an ideal sphere.

On the basis of the autocorrelation analysis, the size of the C6 cells is approximately 20% larger than that of the Y79 cells, i.e., the determined sizes are approximately 7.6 μm for the C6 cells and 6.4 μm for the Y79 cells. From Figure 1, it is not entirely clear that there is a significant size difference between the cells: although the dissociated Trypsin cells of C6 do appear ~20% larger than those of the Y79 cells, the fixed cells appear approximately the same size. We do note that the resolution of optical microscopes is on the order of a micron and, in addition, a slight defocusing can increase the apparent size of the particles significantly. In addition, a microscope images the fields surrounding a particle, not the particle itself. Such external surface fields may be enhanced, depending on the surface roughness of the particle. While defocusing is the most likely reason for the significant size discrepancy between the Trypsin and Fixed Y79 cells, it is difficult to make an accurate size determination less than 1 μm based on such images. The microscope images of Figure 1 can be relied upon to provide only an approximate size and shape estimation.

As a final note, a real cell does not have the morphology of a simple spheroid with a smooth surface and uniform distribution composed of the same material, or have the same refractive index material, and the resulting scattering pattern is much less correlated than the theoretical simulation based on a uniform spheroid. Therefore, the measured ratio between the first and second correlation peak [1.0:0.37 in Figure 4 (a)] shows a faster decay than those of the model particles obtained using the T-matrix calculation [1:0.5 in Figure 5a, and likewise for the corresponding (b) plots]. Nevertheless, the calculations in this section suggest that the scattering patterns of spheres, spheroids, and the actual cells are correlated well enough in their angular structure that they all yield approximately the same secondary-peak positions quantified by Eq. (2).

Discussion

The goal of this experiment is to investigate the possibility of discriminating different cells using flow cytometry without attaching antibody and fluorescent labeling molecules. The experimental methodology allows us to obtain two-dimensional angularly resolved scattering patterns from single cells. We analyze them using autocorrelation techniques. The scattering pattern is determined by the cell's size, shape, refractive index, absorption, orientation, distribution of materials, and surface roughness. While the scattering pattern is sensitive to very small differences in the cell, this sensitivity also makes it difficult to isolate the contribution from each of these parameters. The autocorrelation analysis simplifies the patterns, removing orientation information and fine structure variations, without losing main details of the cell size, shape, and composition. The location of the secondary autocorrelation peak in the theta direction gives the size of an equivalent spheroid with a fixed refractive index; the autocorrelation in the phi direction reveals how closely the cell resembles a sphere;

and the decay rate of the autocorrelation peaks contains information on composition and surface roughness. While these parameters have similar values for the individual C6 or Y79 cells, the differences are large enough between the two kinds of cells to be detected using the autocorrelation techniques.

While the results of this experiment are positive, these are the first experiments in such a flow-through system. The next step is to apply this technology to a real flow cytometry system, in which cells flow through the detection area in buffer liquid and are not subjected to a drying column to evaporate buffer fluid without drying the cell itself. It is expected that this will reduce the contrast of the scattering patterns and make the experiment more difficult, while at the same time removing possible effects of the drying column. Even though our microscopy images show there is no recognizable change in these cells that are collected after passing through the drying column or are dried directly from the liquid media, such a methodology performed without drying is more relevant and practical for laboratory analyses.

In addition to changes in the experimental methodology, a more accurate theoretical model of the cells, including concentric layers of different refractive index media would better enforce this technology. The biological variability of cellular characteristics over populations can be troublesome, and we cannot say whether this technology is sufficient to discriminate individual cells on-the-fly. Such models will assist in determining the sensitivity of the scattering patterns on different parameters.

Summary

The TAOS patterns retrieved from single aerosolized cells contain information about the cell size and morphology. Cell size can be determined readily from the secondary-peak position and it is simple to discriminate, for instance, C6 cells from Y79 cells by using autocorrelation parameters extracted from the TAOS patterns. Further study is required to explore the limitations in discriminating different types of living human cells just from TAOS and intrinsic fluorescence. The constant c in Eq. (2) is expected to depend on the properties of cell morphology, and it is likely that a suitable calibration procedure be developed to determine its value for a desired class of cells. This can be done through numerical calculations for known morphologies or experimentally using known samples. This would enable real-time single-cell sizing using a TAOS-based flow-through apparatus. The use of TAOS patterns and autocorrelation analyses provides a means for classifying cells in a label-free flow cytometry.

Literature Cited

1. Herzenberg LA, Parks D, Sahaf B, Perez O, Roederer M, Herzenberg LA. The history and future of the fluorescence activated cell sorter and flow cytometry: A view from Stanford. Clin Chem 2002;48:1819–1827.
2. Cram LS, Arndt-Jovin D, Fulwyler MJ. Pioneer of flow cytometry and flow sorting (1936–2001). Cytometry A 2005;67:53–60.
3. Kamentsky LA. Cytology automation. In: Lawrence JH, Gofman JW, editors. Advances in Biological and Medical Physics. New York: Academic; 1973.
4. Fulwyler MJ. Electronic separation of biological cells by volume. Science 1965;150: 910–911.
5. Shapiro HM. Practical Flow Cytometry, 4th ed. New Jersey: Wiley; 2002.
6. Goddard G, Martin JC, Naivar M, Goodwin PM, Graves SW, Habbersett R, Nolan JP, Jett JH. Single particle high resolution spectral analysis flow cytometry. Cytometry A 2006;69:842–851.
7. Roederer M. Spectral compensation for flow cytometry: Visualization artifacts, limitations, and caveats. Cytometry B Clin Cytometry 2001;45:194–205.
8. Pan YL, Cobler P, Rhodes S, Potter A, Chou T, Holler S, Chang RK, Pinnick RG, Wolf JP. High-speed, high-sensitivity aerosol fluorescence spectrum detection by using a 32-anode PMT detector. Rev Sci Instruments 2001;72:1831–1836.
9. Pan YL, Chang RK. Multiple-anode PMT behaves like many detectors in one. Laser Focus World 2001;May:235–240.
10. Pan YL, Pinnick RG, Hill SC, Chang RK. Particle-fluorescence spectrometer for real-time measurements of atmospheric organic carbon and biological aerosol. Environ Sci Technol 2009;43:429–434.
11. Kaye PH, Barton JE, Hirst E, Clark JM. Simultaneous light scattering and intrinsic fluorescence measurement for the classification of airborne particles. Appl Opt 2000;39:3738–3745.
12. Hirst E, Kaye PH, Foot V, Clark JM, Withers PB. An instrument for the simultaneous acquisition of size, shape, and spectral fluorescence data from single aerosol particles. Proc SPIE 2004;5617:416–423.
13. Pan YL, Aptowicz KB, Hart M, Eversole JD, Chang RK. Characterizing and monitoring respiratory aerosols by light scattering. Opt Lett 2003;28:589–591.
14. Aptowicz KB, Pinnick RG, Hill SC, Pan YL, Chang RK Optical scattering patterns from single urban aerosol particles at Adelphi. Maryland, USA: A classification relating to particle morphologies. J Geophys Res 2006;111:D12212.
15. Salzman GC, Crowell JM, Goad CA, Hansen KM, Hiebert RD, LaBauve PM, Martin JC, Ingram ML, Mullaney PF. A flow-system multiangle light-scattering instrument for cell characterization. Clin Chem 1975;21:1297–1304.
16. Wyatt PJ. Differential light scattering—A physical method for identifying living bacterial cells. Appl Opt 1968;7:1879–1896.
17. Maltsev VP. Scanning flow cytometetry for individual particle analysis. Rev Sci Instruments 2000;71:243–255.
18. Semyanov KA, Tarasov PA, Zharinov AE, Chernyshev AV, Hoekstra AG, Maltsev VP. Single-particle sizing from light scattering by spectral decomposition. Appl Opt 2004;43:5110–5115.
19. Kaye PH, Aptowicz K, Chang RK, Foot V, Videen G. Angularly resolved elastic scattering from airborne particles. In: Hoekstra A, Maltsev V, Videen G, editors. Optics of Biological Particles. Dordrecht: Kluwer; 2007.
20. Shkuratov Y, Videen G, Kreslavsky M, Belskaya, I, Kaydash V, Ovcharenko A, Omelchenko V, Opanasenko N, Zubko E. Scattering properties of planetary regoliths near opposition. In: Videen G, Yatskiv Y, Mishchenko M, editors. Photopolarimetry in Remote Sensing. Dordrecht: Kluwer; 2004.
21. Auger JC, Aptowicz KB, Pinnick RG, Pan YL, Chang RK. Angularly resolved light scattering from aerosolized spores: Observations and calculations. Opt Lett 2007;32: 3358–3360.
22. Smith PR, Kusmartseva O, Naimimohases R. Evidence for particle-shape sensitivity in the correlation between polarization states of light scattering. Opt Lett 2001;26: 1289–1291.
23. Welford WT. laser speckle and surface roughness. Contemp Phys 1980;21:401–412.
24. Duncan DD, Kirkpatrick SJ. The copula: A tool for simulating speckle dynamics. J Opt Soc Am A 2008;25:231–237.
25. Holoubek J, Krug H, Krepelka J, Hradil Z. Light scattering speckle patterns and their correlation properties. J Mod Opt 1987;34:633–642.
26. Seal K, Sarychev AK, Noh H, Genov DA, Yamilov A, Shalaev VM, Ying ZC, Cao H. Near-field intensity correlations in semicontinuous metal-dielectric films. Phys Rev Lett 2005;94:226101.
27. Cao H, Ling Y, Xu JY, Burin AL. Probing localized states with spectrally resolved speckle techniques. Phys Rev E 2002;66:25601(R).
28. Mishchenko MI, Travis LD, Lacis AA. Scattering, Absorption, and Emission of Light by Small Particles. Cambridge: Cambridge University Press; 2002.
29. Hammer M, Schweitzer D, Michel B, Thamm E, Kolb A. Single scattering by red blood cells. Appl Opt 1998;31:7410–7418.
30. Sorensen CM, Shi D. Patterns in the ripple structure of Mie scattering. J Opt Soc Am A 2002;19:122–125.
31. Bottiger JR, Deluca PJ, Stuebing EW, Vanreenaen DR An ink jet aerosol generator. J Aerosol Sci 1998;29:S965–S966.
32. Franke R, Nielson G. Smooth interpolation of large sets of scattered data. Int J Numer Methods Eng 1980;15:1691–1704.